RSC Advances

PAPER

View Article Online
View Journal | View Issue

Cite this: *RSC Adv.*, 2020, **10**, 22775

$CuCo_2O_4$ nanoneedle array with high stability for high performance asymmetric supercapacitors†

Ling Zhang,[a] Ruizhi Li,*[ab] Weiqun Li,[a] Rongcong Li,[a] Chenliang Li[a] and Yingke Zhou*[a]

Received 27th April 2020
Accepted 2nd June 2020

DOI: 10.1039/d0ra03771k

rsc.li/rsc-advances

Cycling performance is very important to device application. Herein, a facile and controllable approach is proposed to synthesize high stability $CuCo_2O_4$ nanoneedle array on a conductive substrate. The electrode presents excellent performances in a large specific capacitance up to 2.62 F cm^{-2} (1747 F g^{-1}) at 1 mV s^{-1} and remarkable electrochemical stability, retaining 164% even over 70 000 cycles. In addition, the asymmetric supercapacitor assembled with the optimized $CuCo_2O_4$ nanoneedle array (cathode) and active carbon (anode), which exhibits superior specific capacity (146 F g^{-1}), energy density (57 W h kg^{-1}), and cycling stability (retention of 83.9% after 10 000 cycles). These outstanding performances are mainly ascribed to the ordered binder-free nanoneedle array architecture and holds great potential for the new-generation energy storage devices.

1. Introduction

The environmental challenges and the energy crisis have prompted tremendous efforts into the exploitation of energy storage and conversion systems. Supercapacitors, as one of the potential candidates, are characterized by high power density, fast recharge ability, environmental compatibility and so on.[1] The properties of supercapacitors, especially cycling performances, are limited by electrode materials, which greatly restrict their practical application.[2–4] At present, the cycling performance of most reported cathode materials can only reach 5000 cycles, such as Co_3O_4–$NiCo_2O_4$ nanosheets (≈91.11%, 5000 cycles),[5] 3D graphene/ZnO nanorods (≈94.4%, 2300 cycles),[6] coral-like MnO_2 (≈99.7%, 5000 cycles),[7] and $Ni(OH)_2$ nanosheets (≈75%, 3000 cycles).[8] Therefore, fabricating long cycle-life cathode materials greatly affects the practical application of the device.

Transition metal oxides have attracted a lot of attention as promising material for pseudocapacitors due to faradaic redox reactions.[9] However, their low electrical conductivity and structural deformation/dissolution inhibit their application in practical high-rate SCs.[10,11] Spinel copper cobaltite ($CuCo_2O_4$), a ternary transition metal oxide, has been utilized as cathode material with considerably improved performance compared to traditional binary metal oxides,[12–14] ascribed to the multiple oxidation states of both Cu^{2+} and Co^{3+} ions. The high theoretical specific capacity, abundant resources, and non-poisonous grant it a prospective electrode material for supercapacitor.[15,16]

Here, we present a binder-free and shape-controlled strategy to fabricate $CuCo_2O_4$ electrode materials on conductive substrate (Ni foam). The optimized electrode with a nanoneedle array morphology attained a high capacitance of 2.62 F cm^{-2} (1747 F g^{-1}) at 1 mV s^{-1} and an exceptionally long cycling performance (≈164% after 70 000 cycles), superior to the reported cathode materials. The high performance partly attributes to the binder-free ordered nanoneedle array structures. The ordered array provides a direct electron transport, facilitates the electrolyte penetration and reduces the interfacial resistance. Meanwhile, the hierarchical porosity framework (Ni foam) combined with the high mesoporous structure of nanoneedles can greatly increase the specific surface area, improve ion diffusion, facilitate mass transport and alleviate structural damage inside the electrode material.[17,18] Furthermore, the as-assembled asymmetric supercapacitor employing the optimized $CuCo_2O_4$ (cathode) and activated carbon (anode), which can work efficiently in a large operating voltage for 1.8 V and exhibit maximum energy density for 57 W h kg^{-1} with excellent lifespan of retaining 83.9% over 10 000 cycles.

2. Experimental

2.1 Material synthesis

All chemicals were used with no other purification. The Ni foam was first cleaned in HCl and ethanol by sonication for 15 min, respectively, then repeatedly rinsed with deionized water, and dried for use. For a typical synthesis of $CuCo_2O_4$ nanoneedle array, 12 mmol of $CuCl_2 \cdot 6H_2O$, 24 mmol of $CoCl_2 \cdot 6H_2O$ and 112 mmol of urea were mixed in 75 mL deionized water to form

[a]*The State Key Laboratory of Refractories and Metallurgy, Institute of Advanced Materials and Nanotechnology, College of Materials and Metallurgy, Wuhan University of Science and Technology, Wuhan 430081, P. R. China. E-mail: rzli@wust.edu.cn; zhouyk@wust.edu.cn*

[b]*Chongqing Key Laboratory for Advanced Materials & Technologies of Clean Energies, Chongqing 400715, P. R. China*

† Electronic supplementary information (ESI) available. See DOI: 10.1039/d0ra03771k

a transparent pink solution. The obtained homogeneous solution and the pre-cleaned Ni foam were sealed in a Teflon-lined autoclave, subsequently heated to 120 °C and maintained for 10 h. After completion of the reaction, the obtained precursor was taken out and washed using deionized water to remove the redundant materials. Finally, the $CuCo_2O_4$ nanoneedle array was formed by annealing the as-synthesized precursor at 400 °C for 2 h in air atmosphere. The active material mass loading is estimated to 1.5 mg cm^{-2} for the typical sample, denoted as $CuCo_2O_4$-12.

For comparative study, the samples with different concentrations were also fabricated. Similar procedure was followed to prepare different nanostructures by adjusting the reactant concentration. It is noted that the molar ratio of $CuCl_2 \cdot 6H_2O$, $CoCl_2 \cdot 6H_2O$ and urea remains unchanged. The samples can be easily denoted as $CuCo_2O_4$-3, $CuCo_2O_4$-6, $CuCo_2O_4$-9, $CuCo_2O_4$-12 (optimized sample), $CuCo_2O_4$-15, standing for 3 mmol, 6 mmol, 9 mmol, 12 mmol, 15 mmol of $CuCl_2 \cdot 6H_2O$ used in the hydrothermal processes. The active material mass loading is estimated to 0.85 mg cm^{-2}, 1.00 mg cm^{-2}, 1.20 mg cm^{-2}, 2.00 mg cm^{-2} for $CuCo_2O_4$-3, $CuCo_2O_4$-6, $CuCo_2O_4$-9 and $CuCo_2O_4$-15, respectively.

2.2 Material characterizations

The morphological characteristics were observed using scanning electron microscopy (SEM, PHILIPS XL30 TMP). The microstructural characteristics were further obtained by transmission electron microscopy (TEM, UHR JEM-2000 SETM/EDS). The phase characteristics were identified by X'Pert Pro MPD diffractometer (XRD, Cu Kα radiation, $\lambda = 0.15418$ nm). The oxidation states were determined by X-ray photoelectron spectroscopy (XPS, Escalab 250Xi, Thermo) measurements. Nitrogen adsorption/desorption was carried on Autosorb-1-MP/LP instrument. The weight was measured by a semi-micro balance (ESJ200-4B) with a readability of 0.01 mg.

2.3 Electrochemical measurements

All electrochemical performances were characterized *via* Bio-Logic VMP3 electrochemical workstation at ambient temperature. The three-electrode configuration contained reference electrode (Ag/AgCl), counter electrode (platinum plate), the as-synthesized samples (1×1 cm^2) and electrolyte (3 M KOH). EIS measurements were performed in open circuit potential between 0.01 Hz and 100 kHz.

Furthermore, the asymmetric supercapacitor assembled with the optimized $CuCo_2O_4$ nanoneedle array (cathode) and active carbon (anode) were conducted in a two-electrode configuration. To prepare AC electrode, first, the mixture with 80 wt% of AC powder, 10 wt% of polyvinylidene fluoride and 10 wt% of carbon black was added appropriate amount of NMP solvent and stirred for 12 h. Then, the obtained homogeneous slurry was drawn and dripped over the nickel foam with a pipetting gun, followed by drying for 12 h at 80 °C and pressed at 10 MPa. The mass loading of AC powder attached to the nickel foam within a 1 cm × 1 cm area is 5.55 mg.

The areal capacitance (C_a) was figured out by the eqn (1):

$$C_a = \left(\int I(V)\mathrm{d}V\right) \Big/ 2\nu VA \quad (1)$$

where $I(V)$ refers to the current at V, dV denotes differential potential, ν represents scan rate, V denotes the potential window, and A is the electrode's surface area.

The specific capacitance (C), energy densities (E) and the power density (P) were figured out by the eqn (2)–(4):

$$C = (I \times \Delta t)/m\Delta V \quad (2)$$

$$E = (C \times \Delta V^2)/7.2 \quad (3)$$

$$P = (E \times 3600)/\Delta t \quad (4)$$

where I is the discharge current, Δt denotes discharge time, m represents the loading mass, and ΔV denotes the applied potential window.

3. Results and discussion

3.1 Characterization analysis

As illustrated in Fig. 1, it is the synthesis process of $CuCo_2O_4$ nanoneedle array. A simple hydrothermal procedure was first performed to obtain Cu–Co nanoneedle array precursor (Fig. 1b) vertically grown on conductive substrate (Ni foam), and then an annealing treatment was carried out to form $CuCo_2O_4$ nanoneedle array (Fig. 1c). As shown in the optical image, the color of Cu–Co precursor and $CuCo_2O_4$ sample turned from pink to black (inset in Fig. 2a). The SEM characterizations were performed to analysis the morphologies for the samples.

Different morphologies were obtained by adjusting concentration of the solvent. With the increase of the reactant concentration, the samples change from nanosheet-like morphology (Fig. S1a†) to nanowire (Fig. S1b and c†), then to a typical uniform and regular nanoneedle array structure (Fig. 2c), and then to a mixed state of sheet and nanoneedle (Fig. S1d†). In $CuCo_2O_4$-12 sample, high density and uniform nanoneedles were vertically grown on Ni foam, ensuring a high utilization for the active material. Fig. 2a, b and c depict SEM images of Cu–Co precursor and $CuCo_2O_4$-12, respectively. After annealing, the obtained nanomaterials turn from a typical vertically needle-like morphology to a porous nanoneedles array formed with nanoparticles. The detailed feature and the structures of $CuCo_2O_4$

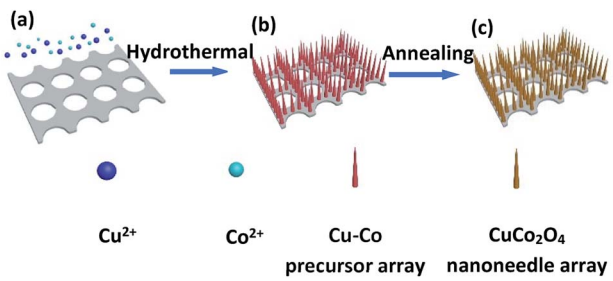

Fig. 1 Schematic evolution process of $CuCo_2O_4$ nanoneedle array on Ni foam: (a) Ni foam and copper, cobalt sources, (b) Cu–Co precursor array and (c) $CuCo_2O_4$ nanoneedle array.

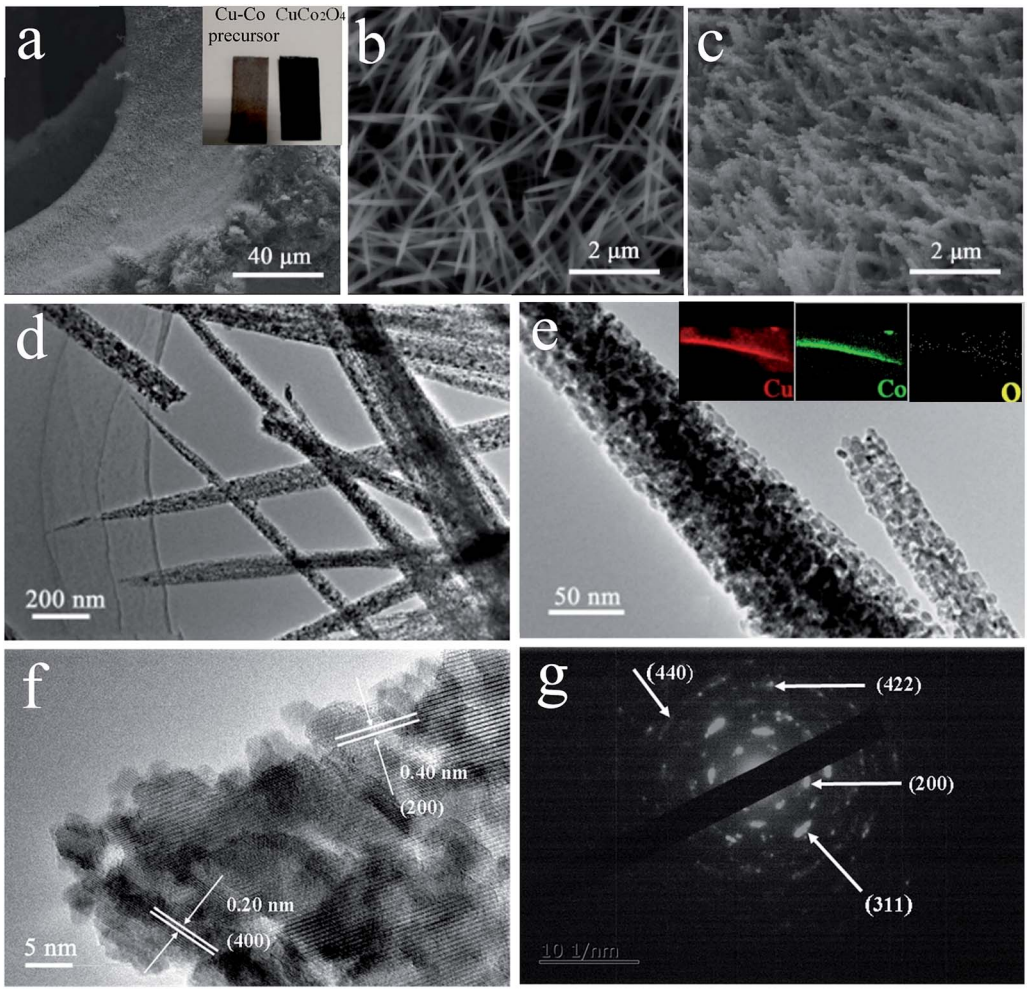

Fig. 2 SEM images of Cu–Co precursor (a and b) and $CuCo_2O_4$ nanoneedle array (c), respectively. TEM images (d–f) and corresponding SAED pattern (g) of $CuCo_2O_4$ nanoneedle array, respectively (inset in (a) is the optical image of Cu–Co precursor and $CuCo_2O_4$ nanoneedle array, insets in (e) are EDX elemental mappings of $CuCo_2O_4$ nanoneedle array).

were further revealed in TEM. The diameter of the $CuCo_2O_4$ nanoneedle is around 50–80 nm and apparent pores are found on the nanoneedle, as shown in Fig. 2d and e. EDX analysis (insets of Fig. 2e) clearly reveals the existence of Cu, Co, O, along with Ni elements, uniformly distributed throughout the nanoneedle. Nanoneedle structure was made up of sizable amounts of dense pores, which benefits to facilitate the ion and electron transportation into active materials, improving the capacitive performance. As displayed in Fig. 2f, the high-resolution TEM image shows the well-defined interplanar *d*-spacings of 0.20 nm for (400) plane and 0.40 nm for (200) plane, which indexed well to the feature of $CuCo_2O_4$. Moreover, the discontinuous SAED pattern (Fig. 2g) further confirms the $CuCo_2O_4$ phase and corroborate the polycrystalline nature of the material.

The composition and phase purity of $CuCo_2O_4$-12 was characterized by XRD (Fig. 3). To avoid the intense peaks of Ni-foam, we performed the XRD analysis of some powder scrapped off from the Ni foam. Diffraction peaks at 19.0, 31.3, 36.8, 38.6, 44.9, 55.8, 59.3, 65.4 and 77.6° could be well indexed to the (111), (220), (311), (222), (40 0), (422), (511), (440), and (553) planes of cubic $CuCo_2O_4$ (JCPDS no. 71-0816). In addition, the absence of other impurity peaks was detected, which confirms the high-purity of the prepared sample.

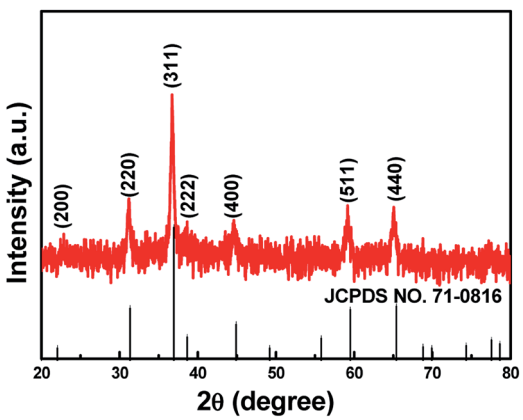

Fig. 3 XRD pattern of $CuCo_2O_4$ nanoneedle array scrapped off from the Ni foam.

Further information on the composition and oxidation state of $CuCo_2O_4$ nanoneedle array were analyzed by XPS spectrum. The characteristic peaks of C, Ni, Cu, Co and O elements are presented in the full survey spectrum (Fig. 4a). As shown in Fig. 4b, the spectrum of Cu 2p illustrates two main peaks located at 933.3 eV and 953.5 eV, which corresponds to Cu $2p_{3/2}$ and Cu $2p_{1/2}$. In addition, two satellite of 941.6 and 961.8 eV confirms Cu^{2+} characteristic.[19,20] The peaks of Co 2p spectrum (Fig. 4c) observed at 779.7 eV (Co $2p_{3/2}$) and 794.7 eV (Co $2p_{1/2}$), along with a splitting of approximately 15 eV, are attributed to the Co^{2+} and Co^{3+} states.[21] The spectrum of the O 1s (Fig. 4d) displays three different oxygen contributions located at 529.4, 531.0 and 532.2 eV, which are ascribed to typical metal–oxygen (Cu–O or Co–O) bonds,[22] the presence of defect sites,[23] and the physically and chemically absorbed hydroxyl groups within the surface of $CuCo_2O_4$ nanoneedle,[24] respectively.

The specific surface area and pore volume of active material play a significant effect on electrochemical properties.[25–27] Fig. 5 represents the BET profile of Cu–Co precursor and $CuCo_2O_4$ nanoneedle array scrapped off from the Ni foam. The curve of the $CuCo_2O_4$ nanoneedle array shows typical IV isotherm, which indicates the unique properties of mesoporous materials.[28] The specific surface area of the $CuCo_2O_4$ nanoneedle array according to BET measurement is 35.18 $m^2\ g^{-1}$, which is much larger than Cu–Co precursor array (10.33 $m^2\ g^{-1}$), attributed to the highly porous structure consistent with the SEM and TEM results. In addition, the pore volume of $CuCo_2O_4$ nanoneedle array (0.174 $cm^3\ g^{-1}$) with average pore diameter of 20.3 nm is much superior to Cu–Co precursor array (0.039 $cm^3\ g^{-1}$). The high surface area combined with the abundant mesoporous structure increases active sites and provides fast mass transport, contributing to excellent electrochemical properties.

3.2 Electrochemical performance

The electrochemical behaviors were first measured in a three-electrode system to evaluate the as-synthesized samples. Cyclic voltammetry (CV) tests within the potential rage between

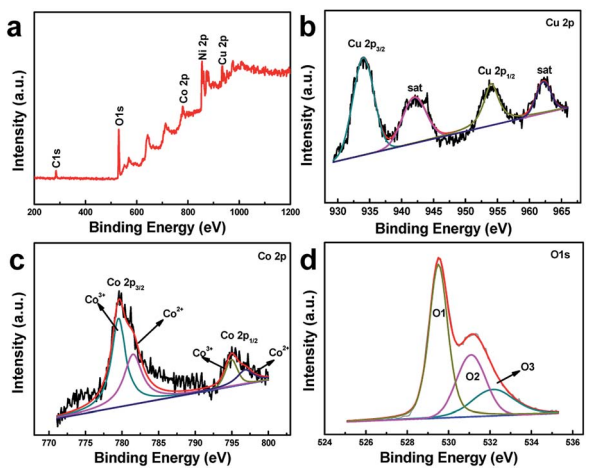

Fig. 4 XPS spectra of survey scan (a), Cu 2p (b), Co 2p (c), and O 1s (d) for $CuCo_2O_4$ nanoneedle array.

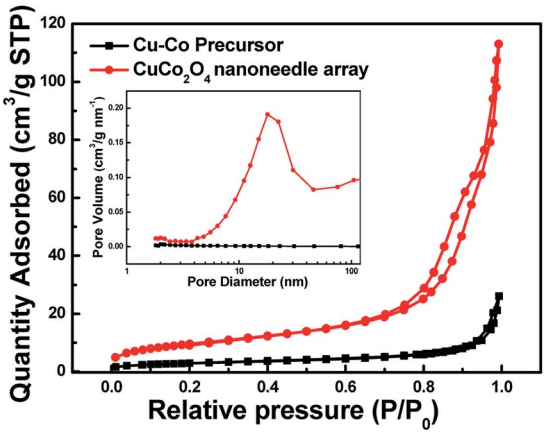

Fig. 5 BET isotherm of Cu–Co precursor and $CuCo_2O_4$ nanoneedle array (inset is the BJH pore size distribution curves).

0 and 0.6 V were obtained. Fig. 6a shows the CV profiles for $CuCo_2O_4$-12 electrode at various sweep rates (CVs of other electrodes are shown in Fig. S2†). The obvious pseudocapacitive behavior was demonstrated by the well-defined redox peaks, attributed to the faradaic reaction associated with Co^{4+}/Co^{3+} and Cu^{2+}/Cu^{+}.[29] Moreover, the shape of the CV profiles is almost invariable and symmetrical during different scan rates, indicating the rapid transfer of electrons, high coulombic efficiency and perfect reversibility of the electrode.[30,31] The corresponding reaction mechanism of $CuCo_2O_4$ during redox reaction in KOH electrolyte is commonly as follows:[32]

$$CuCo_2O_4 + H_2O + e^- \leftrightarrow 2CoOOH + CuOH \quad (5)$$

$$CoOOH + OH^- \leftrightarrow CoO_2 + H_2O + e^- \quad (6)$$

$$CuOH + OH^- \leftrightarrow Cu(OH)_2 + e^- \quad (7)$$

The galvanostatic charge–discharge (CD) curves were depicted in Fig. 6b. All these curves show nearly symmetric shapes, revealing good electrochemical reversibility. The obvious plateau reveals a more significant battery-type redox behavior, consistent with the CV curves result. Fig. 6c displays the CV comparisons for all as-prepared electrodes attained from different concentration at 20 mV s^{-1}. All curves exhibit the similar pairs of redox peaks. The largest CV integrated area of $CuCo_2O_4$-12 electrode obviously indicates highest capacitance than others. To learn more about this, Fig. 6d displays the detailed capacitance *versus* scan rate for electrode with different reactant concentration. The results reveal that $CuCo_2O_4$-12 electrode delivers higher areal capacitance than others at all scan rates. $CuCo_2O_4$-12 electrode displays highest capacitance of 2.620 F cm^{-2} at 1 mV s^{-1} ($CuCo_2O_4$-3: 1.176 F cm^{-2}; $CuCo_2O_4$-6: 1.252 F cm^{-2}; $CuCo_2O_4$-9: 1.298 F cm^{-2}; $CuCo_2O_4$-15: 1.667 F cm^{-2}), demonstrating outstanding charge storage. Meanwhile, $CuCo_2O_4$-12 electrode maintains 0.81 F cm^{-2} at 100 mV s^{-1} ($CuCo_2O_4$-3: 0.430 F cm^{-2}; $CuCo_2O_4$-6: 0.407 F cm^{-2}; $CuCo_2O_4$-9: 0.412 F cm^{-2}; $CuCo_2O_4$-15: 0.537 F cm^{-2}), indicating good

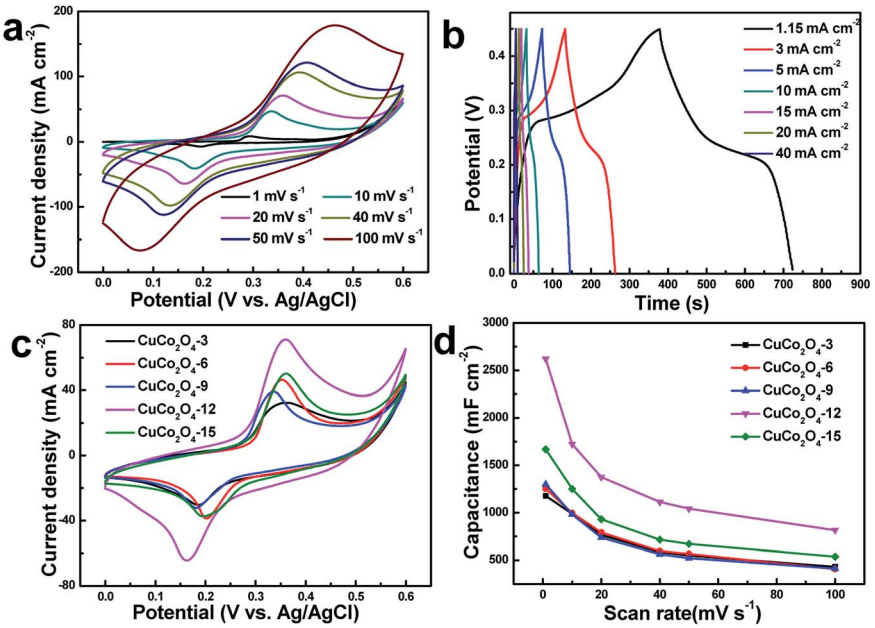

Fig. 6 (a) CV curves for $CuCo_2O_4$-12 electrode at different sweep rates, (b) CD curves for $CuCo_2O_4$-12 electrode at different current densities, (c) CV curves for electrodes of different concentrations at 20 mV s^{-1}, (d) variations of capacitance with scan rate for electrodes of different concentrations.

rate performance. In addition, the curve of capacitance shows a decreasing trend, which is ascribe to the insufficient diffusion of OH^- ions with increasing the scan rate.[33] The better electrochemical properties of $CuCo_2O_4$-12 electrode are attributed to the mesoporous nanoneedle array architecture, which provides a direct electron transport, facilitates the electrolyte penetration and reduces the interfacial resistance.[34,35] The above evidence implies that proper reactant concentration leads to better nanostructure and higher electrochemical performance.

With the optimized nanoarchitecture ($CuCo_2O_4$-12), the most remarkable performance improvement is the long-term cycling stability. As shown in Fig. 7a, 70 000 cycles were tested at 50 mV s^{-1}. Impressively, the capacity retention of the $CuCo_2O_4$-12 electrode remains ≈164% after 70 000 cycles. The capacitance gets increased at first and keep almost stable in following cycles. The increasing tendency of cycling curve attributed to the activation process and enhanced participated electroactive surface area.[36,37] This result is much superior to the reported $CuCo_2O_4$ electrodes, for instance, $CuCo_2O_4$ nanowires (≈100.9%, 10 000 cycles),[38] $CuCo_2O_4$ flowers (≈109%, 2000 cycles),[39] $CuCo_2O_4$ nanosheets (≈79.7%, 5000 cycles),[40] onion-like nanoporous $CuCo_2O_4$ hollow spheres (≈93.4%, 5000 cycles),[41] and $CuCo_2O_4$ nanobelts (≈127%, 1800 cycles)[42] in alkaline electrolyte. The capacity retention (exceeds 100%) could be explained in two aspects: the synergistic effects of Cu, Co redox reactions and the hierarchical porous structures of $CuCo_2O_4$ materials. At first stage, the electrochemical reactions mainly occurred on the surface of the $CuCo_2O_4$ materials. With the cycle increased, the internal active materials were gradually activated, thereby increasing the active site. Meantime, the mesoporous structure of nanoneedles buffers structural deformation, helping maintain the structural stability.[43] Moreover, the nanoneedle array structure contribute abundant electrochemical active sites and shorten the diffusion length, enhancing long-term cycling stability. To further understand the fundamental behavior of cycling process, the electrochemical impedance spectroscopy (Fig. 7b) was measured. In EIS spectrum, the *x*-axis intercept of the curve and the diameter of semicircle stand for the series resistance and charge-transfer

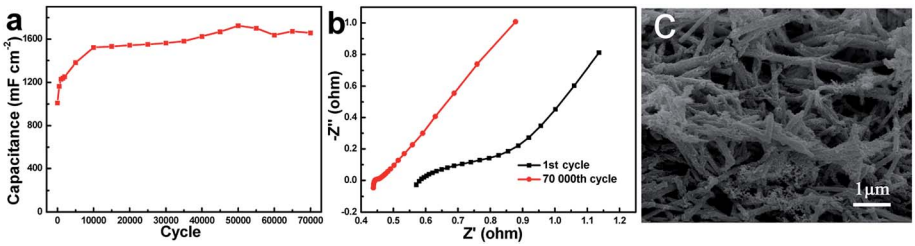

Fig. 7 (a) Cycling performances, (b) EIS spectra before and after cycle testing, (c) SEM image after 70 000 cycles of the $CuCo_2O_4$-12 electrode.

resistance. It is observed that electrode after 70 000 cycles exhibits smaller R_s and R_{ct} (after R_s: 0.44 Ω, R_{ct}: 0.02 Ω; before R_s: 0.58 Ω, R_{ct}: 0.8 Ω), indicating improved electrical conductivity. In addition, the higher slope (after cycling) of the spike line observed at low frequency reveals the more easily ion diffusion. For comparison, Fig. 7c shows the SEM image after 70 000 cycles. It is observed that the porous nanoneedle morphology can still be well preserved although regular array architecture has changed. The good electrochemical performance especially excellent stability over thousands of long cycles demonstrates that the optimized electrode is promising for practical applications.

3.3 Fabrication of asymmetric supercapacitor

To further demonstrate the practical feasibility of the optimized $CuCo_2O_4$-12 electrode, an asymmetric supercapacitor $CuCo_2O_{4(+)}//AC_{(-)}$ was constructed with 3 M KOH. The CV profiles of the AC and $CuCo_2O_4$-12 electrodes at 20 mV s^{-1} are displayed in Fig. 8a. Rectangular profile of AC anode reveals the electric double-layer capacitive behavior which is different from the electrochemical feature of $CuCo_2O_4$ cathode. Fig. 8b displays that the asymmetric supercapacitor can work efficiently in a large operating voltage for 1.8 V, which is superior to many reported aqueous asymmetric supercapacitors (1.4–1.6 V). As shown, the curves of device maintain a nearly rectangular-like shape in various scan rates, indicating good reversible ability and ideal capacitance behavior. The discharge curves (Fig. 8c) show that the potential decay is linear at the beginning and then slows down. The corresponding specific capacitances *versus* current densities are presented in Fig. 8d. Notably, the asymmetric supercapacitor can reach 146 F g^{-1} (0.5 A g^{-1}) and retain 42 F g^{-1} with increasing to 14.3 A g^{-1}, implying good rate ability.

Ragone plots are important for device application. The Ragone plots of $CuCo_2O_{4(+)}//AC_{(-)}$ device based on CD curves are shown in Fig. 8e. The asymmetric supercapacitor delivers a maximum energy density of 57 W h kg^{-1} at 420 W kg^{-1}, which outperforms those of aqueous asymmetric devices reported recently, such as AC//$CuCo_2O_4$/CuO (18 W h kg^{-1}),[44] $CuCo_2O_4$@$CuCo_2O_4$//AC (18 W h kg^{-1}),[45] $CuCo_2O_4$@$Co(OH)_2$//GA (19.2 W h kg^{-1}),[46] AC//$CuCo_2O_4$@$Ni(OH)_2$ (48 W h kg^{-1}),[47] AC//Co_3O_4@$Ni(OH)_2$ (40 W h kg^{-1}),[48] AC//NiCoP@C@$Ni(OH)_2$ (49.5 W h kg^{-1}),[49] $NiCo_2O_4$//AC (6.8 W h kg^{-1}),[50] and AC//MnO_2 (30.6 W h kg^{-1}).[51] Moreover, the device remains 16.8 W h kg^{-1} at 12 142 W kg^{-1}, revealing a well power ability. Additionally, the cycling performance of the as-fabricated asymmetric

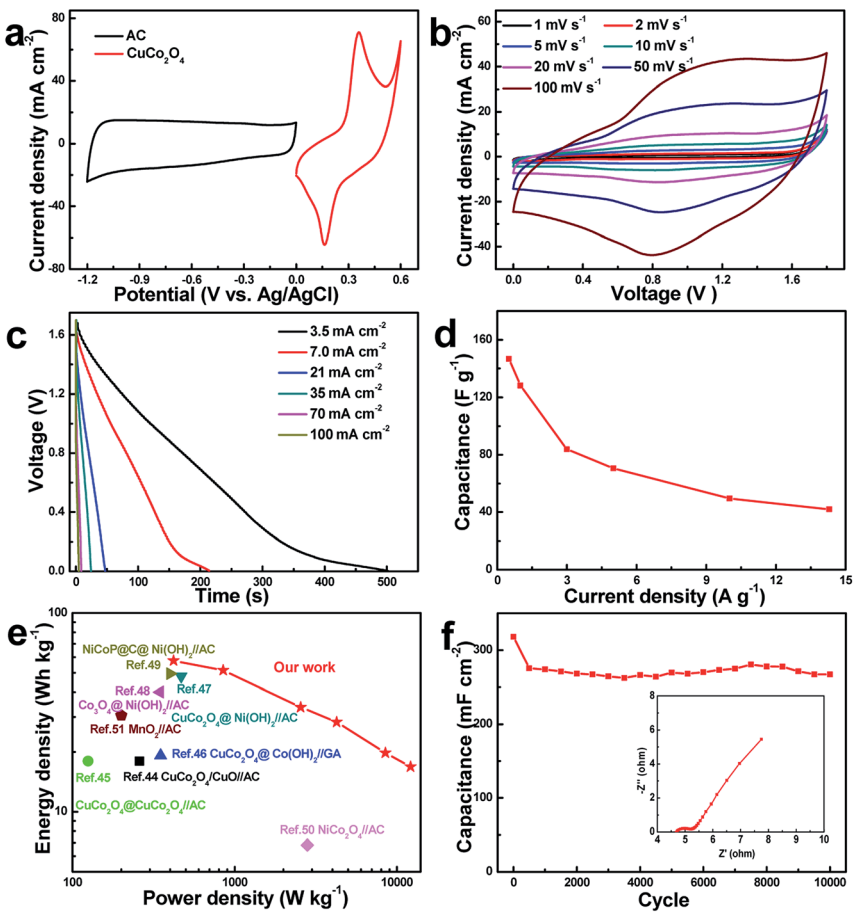

Fig. 8 The $CuCo_2O_{4(+)}//AC_{(-)}$ device: (a) comparative CV profiles for $CuCo_2O_4$-12 and AC electrode at 20 mV s^{-1}, (b) CV curves, (c) discharge curves, (d) capacitance behaviors *versus* current density, (e) Ragone plots and (f) cycling stability.

supercapacitor was performed at 50 mV s^{-1}. After 10 000 cycles (Fig. 8f), the capacitance shows 83.9% retention of initial capacitance, implying excellent cycling performance, much better than the reported asymmetric devices, for instance, MnO_2@carbon spheres//nitrogen-doped activated carbon (≈74.4%, 1000 cycles),[52] Co_3O_4@Ni_3S_2//AC (≈61.5%, 1000 cycles),[53] CoMn-layered double hydroxides//Fe_3O_4@N-doped carbon (≈80%, 5000 cycles),[54] and ZnO nanoflakes//AC (≈75.6%, 8000 cycles).[55] The EIS testing of the device (inset in Fig. 8f) was further performed to understand the electrochemical behavior. The *x*-axis intercept of the curve (R_s) and the diameter of semicircle (R_{ct}) are 4.7 Ω and 0.55 Ω, respectively, which reveals a small intrinsic resistance of the electrochemical system and rapid transport kinetics of electron. Furthermore, the steep slope of the linear portion indicates an efficient ionic diffusion. The above results endow great application potentials of our device in electrochemical capacitor.

4. Conclusions

In summary, the mesoporous $CuCo_2O_4$ nanoneedle array was successfully fabricated *via* a facile and controllable hydrothermal technique, for which the structure and electrochemical performance can be controlled by simply adjusting reactant concentration. Meantime, the optimized $CuCo_2O_4$-12 electrode exhibits a superb storage capacity of 2.62 F cm^{-2} (1747 F g^{-1}) with remarkable cyclic stability (164% retention over 70 000 cycles). Moreover, the fabricated $CuCo_2O_4$//AC asymmetric supercapacitor achieved an ultrahigh energy density of 57 W h kg^{-1} and excellent cyclic stability retained 83.9% after 10 000 cycles. These outstanding performances indicate that the optimized mesoporous $CuCo_2O_4$ nanoneedle array electrode holds great potential in energy storage applications.

Conflicts of interest

There are no conflicts to declare.

Acknowledgements

This work was supported by the National Natural Science Foundation of China (No. 51802233), the Natural Science Foundation of Hubei Province of China (No. 2018CFB154, 2018CFA022) and Chongqing Key Laboratory for Advanced Materials & Technologies of Clean Energies (No. JJNY201906).

Notes and references

1 W. Raza, F. Ali, N. Raza, Y. Luo, K.-H. Kim, J. Yang, S. Kumar, A. Mehmood and E. E. Kwon, *Nano Energy*, 2018, **52**, 441–473.
2 J. Lin, H. Jia, H. Liang, S. Chen, Y. Cai, J. Qi, C. Qu, J. Cao, W. Fei and J. Feng, *Adv. Sci.*, 2018, **5**, 1700687.
3 X. Zhang, S. Deng, Y. Zeng, M. Yu, Y. Zhong, X. Xia, Y. Tong and X. Lu, *Adv. Funct. Mater.*, 2018, **28**, 1805618.
4 X. Wang, B. Liu, R. Liu, Q. Wang, X. Hou, D. Chen, R. Wang and G. Shen, *Angew. Chem., Int. Ed.*, 2014, **53**, 1849–1853.
5 D. Chen, D. Pang, S. Zhang, H. Song, W. Zhu and J. Zhu, *Electrochim. Acta*, 2020, **330**, 135326.
6 X. Li, Z. Wang, Y. Qiu, Q. Pan and P. Hu, *J. Alloys Compd.*, 2015, **620**, 31–37.
7 M. Cakici, K. R. Reddy and F. Alonso-Marroquin, *Chem. Eng. J.*, 2016, **309**, 151–158.
8 X. Xiong, D. Ding, D. Chen, G. Waller, Y. Bu, Z. Wang and M. Liu, *Nano Energy*, 2015, **11**, 154–161.
9 Q. Gao, J. Wang and J. Wang, *J. Alloys Compd.*, 2019, **789**, 193–200.
10 G. Xiong, P. He, D. Wang, Q. Zhang, T. Chen and T. S. Fisher, *Adv. Funct. Mater.*, 2016, **26**, 5460–5470.
11 W. Fu, L. Long, M. Wang, Y. Yao, N. Wei, M. Yan, G. Yin, X. Liao, Z. Huang and X. Chen, *J. Alloys Compd.*, 2015, **631**, 82–85.
12 A. Pendashteh, S. E. Moosavifard, M. S. Rahmanifar, Y. Wang, M. F. El-Kady, R. B. Kaner and M. F. Mousavi, *Chem. Mater.*, 2015, **27**, 3919–3926.
13 A. T. Aqueel Ahmed, B. Hou, H. S. Chavan, Y. Jo, S. Cho, J. Kim, S. M. Pawar, S. Cha, A. I. Inamdar, H. Kim and H. Im, *Small*, 2018, **14**, e1800742.
14 F. S. Omar, A. Numan, N. Duraisamy, M. M. Ramly, R. Kasi and R. T. Subramaniam, *Electrochim. Acta*, 2017, **227**, 41–48.
15 L. Abbasi and M. Arvand, *Appl. Surf. Sci.*, 2018, **445**, 272–280.
16 Y. Wang, D. Yang, J. Lian, T. Wei and Y. Sun, *J. Alloys Compd.*, 2018, **741**, 527–531.
17 B. Fang, J. H. Kim, M.-S. Kim, A. Bonakdarpour, A. Lam, D. P. Wilkinson and J.-S. Yu, *J. Mater. Chem.*, 2012, **22**, 19031–19038.
18 Y. Z. Wei, B. Fang, S. Iwasa and M. Kumagai, *J. Power Sources*, 2005, **141**, 386–391.
19 S. E. Moosavifard, S. Fani and M. Rahmanian, *Chem. Commun.*, 2016, **52**, 4517–4520.
20 R. BoopathiRaja, M. Parthibavarman and A. Nishara Begum, *Vacuum*, 2019, **165**, 96–104.
21 F. Saleki, A. Mohammadi, S. E. Moosavifard, A. Hafizi and M. R. Rahimpour, *J. Colloid Interface Sci.*, 2019, **556**, 83–91.
22 S. K. Kaverlavani, S. E. Moosavifard and A. Bakouei, *J. Mater. Chem. A*, 2017, **5**, 14301–14309.
23 X.-F. Lu, D.-J. Wu, R.-Z. Li, Q. Li, S.-H. Ye, Y.-X. Tong and G.-R. Li, *J. Mater. Chem. A*, 2014, **2**, 4706–4713.
24 C. Jin, Y. Cui, G. Zhang, W. Luo, Y. Liu, Y. Sun, Z. Tian and W. Zheng, *Chem. Eng. J.*, 2018, **343**, 331–339.
25 B. Fang, M. Kim, S. Q. Fan, J. H. Kim, D. P. Wilkinson, J. Ko and J. S. Yu, *J. Mater. Chem.*, 2011, **21**, 8742–8748.
26 B. Fang, J. H. Kim, M. S. Kim and J. S. Yu, *Acc. Chem. Res.*, 2013, **46**, 1397–1406.
27 W. B. Hua, X. D. Guo, Z. Zheng, Y. J. Wang, B. H. Zhong, B. Fang, J. Z. Wang, S. L. Chou and H. Liu, *J. Power Sources*, 2015, **275**, 200–206.
28 J. Xie, Z. Zhan, S. Zhang, G. Li, H. Xia, Y. Yang and J. Xiong, *Mater. Lett.*, 2018, **226**, 30–33.
29 S. Kamari Kaverlavani, S. E. Moosavifard and A. Bakouei, *Chem. Commun.*, 2017, **53**, 1052–1055.
30 Y. Zhu, X. Pu, W. Song, Z. Wu, Z. Zhou, X. He, F. Lu, M. Jing, B. Tang and X. Ji, *J. Alloys Compd.*, 2014, **617**, 988–993.

31 Y. Tang, Y. Liu, S. Yu, Y. Zhao, S. Mu and F. Gao, *Electrochim. Acta*, 2014, **123**, 158–166.
32 S. Vijayakumar, S. Nagamuthu and G. Muralidharan, *ACS Sustainable Chem. Eng.*, 2013, **1**, 1110–1118.
33 R. Suresh Babu, R. Vinodh, A. L. F. de Barros, L. M. Samyn, K. Prasanna, M. A. Maier, C. H. F. Alves and H.-J. Kim, *Chem. Eng. J.*, 2019, **366**, 390–403.
34 J. H. Kim, B. Fang, M. Kim and J. S. Yu, *Catal. Today*, 2009, **146**, 25–30.
35 B. Fang, S. Q. Fan, J. H. Kim, M. S. Kim, M. Kim, N. K. Chaudhari, J. Ko and J. S. Yu, *Langmuir*, 2010, **26**, 11238–11243.
36 S. Vijayakumar, S.-H. Lee and K.-S. Ryu, *Electrochim. Acta*, 2015, **182**, 979–986.
37 X. Tang, H. Li, Z. H. Liu, Z. Yang and Z. Wang, *J. Power Sources*, 2011, **196**, 855–859.
38 L. Liao, H. Zhang, W. Li, X. Huang, Z. Xiao, K. Xu, J. Yang, R. Zou and J. Hu, *J. Alloys Compd.*, 2017, **695**, 3503–3510.
39 S. Vijayakumar, S. Nagamuthu and K.-S. Ryu, *Electrochim. Acta*, 2017, **238**, 99–106.
40 S. Liu, K. S. Hui and K. N. Hui, *ACS Appl. Mater. Interfaces*, 2016, **8**, 3258–3267.
41 A. A. Ensafi, S. E. Moosavifard, B. Rezaei and S. K. Kaverlavani, *J. Mater. Chem. A*, 2018, **6**, 10497–10506.
42 B. Sydulu Singu, R. Kuchi, P. Cao Van, D. Kim, K. Ro Yoon and J. Ryul Jeong, *ChemNanoMat*, 2019, **5**, 1398–1407.
43 B. Fang, H. Zhou and I. Honma, *J. Phys. Chem. B*, 2006, **110**, 4875–4880.
44 A. Shanmugavani and R. K. Selvan, *Electrochim. Acta*, 2016, **188**, 852–862.
45 Y. Zhang, J. Xu, Y. Zheng, Y. Zhang, X. Hu and T. Xu, *RSC Adv.*, 2017, **7**, 3983–3991.
46 Y. Zhang, H. Liu, M. Huang, J. M. Zhang, W. Zhang, F. Dong and Y. X. Zhang, *ChemElectroChem*, 2017, **4**, 721–727.
47 Z. Zhan, S. Chen, J. Xie, Y. Yang and J. Xiong, *J. Alloys Compd.*, 2017, **722**, 928–937.
48 X. Bai, Q. Liu, J. Liu, H. Zhang, Z. Li, X. Jing, P. Liu, J. Wang and R. Li, *Chem. Eng. J.*, 2017, **315**, 35–45.
49 Q. Zong, H. Yang, Q. Wang, Q. Zhang, Y. Zhu, H. Wang and Q. Shen, *Chem. Eng. J.*, 2019, **361**, 1–11.
50 R. Ding, L. Qi, M. Jia and H. Wang, *Electrochim. Acta*, 2013, **107**, 494–502.
51 J.-G. Wang, Y. Yang, Z.-H. Huang and F. Kang, *Carbon*, 2013, **61**, 190–199.
52 J. Wen, X. Chen, M. Huang, W. Yang and J. Deng, *J. Chem. Sci.*, 2019, **132**, 1–11.
53 X. X. Liu, R. Wu, Y. Wang, S. H. Xiao, Q. He, X. B. Niu, D. J. Blackwood and J. S. Chen, *Electrochim. Acta*, 2019, **311**, 221–229.
54 J. Zhou, S. Xu, L. Ni, N. Chen, X. Li, C. Lu, X. Wang, L. Peng, X. Guo, W. Ding and W. Hou, *J. Power Sources*, 2019, **438**, 227047.
55 A. Ali, M. Ammar, M. Ali, Z. Yahya, M. Y. Javaid, S. U. Hassan and T. Ahmed, *RSC Adv.*, 2019, **9**, 27432–27438.

